New method for shadow calculations: Application to parametrized axisymmetric black holes

Ziri Younsi,[1] Alexander Zhidenko,[2,1] Luciano Rezzolla,[1,3] Roman Konoplya,[1] and Yosuke Mizuno[1]

[1]*Institute for Theoretical Physics, Goethe-University, Max-von-Laue-Str. 1, 60438 Frankfurt, Germany*
[2]*Centro de Matemática, Computação e Cognição, Universidade Federal do ABC (UFABC),*
Rua Abolição, CEP: 09210-180 Santo André, SP, Brazil
[3]*Frankfurt Institute for Advanced Studies, Ruth-Moufang-Str. 1, D-60438 Frankfurt am Main, Germany*

Collaborative international efforts under the name of the Event Horizon Telescope project, using sub-mm very long baseline interferometry, are soon expected to provide the first images of the shadow cast by the candidate supermassive black hole in our Galactic center, Sagittarius A*. Observations of this shadow would provide direct evidence of the existence of astrophysical black holes. Although it is expected that astrophysical black holes are described by the axisymmetric Kerr solution, there also exist many other black hole solutions, both in general relativity and in other theories of gravity, which cannot presently be ruled out. To this end, we present calculations of black hole shadow images from various metric theories of gravity as described by our recent work on a general parametrization of axisymmetric black holes [R. Konoplya, L. Rezzolla, and A. Zhidenko, Phys. Rev. D **93**, 064015 (2016).]. An algorithm to perform general ray-tracing calculations for any metric theory of gravity is first outlined and then employed to demonstrate that even for extremal metric deformation parameters of various black hole spacetimes, this parametrization is both robust and rapidly convergent to the correct solution.

I. INTRODUCTION

It is now widely believed that at the center of every galaxy resides a supermassive black hole. Observational evidence, particularly for our own galactic black hole candidate, Sagittarius A* (Sgr A*), is compelling [1,2] and supports the notion of an object of enormous density, most likely a supermassive black hole, residing in the innermost central region.

However, direct observation of an astrophysical black hole remains illusive, and this is because of the existence of the event horizon, that is, a surface limiting a region of spacetime beyond which neither matter nor radiation can escape the gravity of the black hole. Outside this surface, but still in close proximity to the event horizon, lies the photon-capture region, where photons follow unstable orbits. Hence, when observing a black hole directly, we expect to see a "silhouette" of this photon region. Therefore, black holes are expected to be observed as a shadow on the background sky [3–5].

It is anticipated that submillimeter very long baseline interferometry (VLBI) observations of Sgr A* with the Event Horizon Telescope [6–8] will soon yield the first radio images of the shadow of the candidate black hole therein. The Black Hole Camera project, in addition to other scientific activities, participates actively in the investigation of the physics and astrophysics of the black hole candidate associated to Sgr A*. Particular attention is dedicated to theoretical calculations of the shadows, whose size and shape are sensitive to certain system parameters, in particular, the black hole mass and spin, as well as the orientation of the spin axis of the black hole with respect to Earth (see, e.g., Ref. [9]). Observations of this shadow would not only provide very compelling evidence for the existence of an event horizon, but also enable estimates to be placed on these system parameters.

While astrophysical black holes are expected to be described by the Kerr solution, there exist numerous black hole solutions in other theories of gravity (see, for example, [10,11] and references therein). One cannot yet exclude the possibility of many of the black hole metrics available in the literature and as such they are all, in a sense, potential candidates. Rather than investigate all possible theories of gravity and their corresponding black hole solutions one at a time, it is expedient to instead consider a model-independent framework within which any particular solution to any theory of gravity may be parametrized through a finite number of modifiable parameters. These parameters can then be chosen to measure deviations from the Kerr metric and may be estimated from astrophysical observations [12].

There is a simple reason why this avenue is a viable one, and although it is quite obvious, it may be useful to recall it here. The problem of defining the properties of the shadow does not require the choice of a theory of gravity, but only of a well-behaved expression for the metric tensor. This is because all that is ultimately needed to compute a shadow is the solution of the geodesic equations. The latter obviously do not require any assumption on the

theory of gravity, but only a well-defined and regular definition of the metric tensor.

In Ref. [13], such a parametric framework was introduced to describe the spacetime of spherically symmetric and slowly rotating black holes in generic metric theories of gravity. The parametrization in [13] is based on a continued fraction expansion in terms of a compactified radial coordinate. Building upon the framework of [13] to also include axisymmetric spacetimes, Ref. [14] presented a parametric description of axisymmetric black holes in generic metric theories of gravity. This new parametrization is based on a double expansion in both the radial and polar directions of a general stationary and axisymmetric metric, and is practically independent of any specific metric theory of gravity. Although it was shown to accurately reproduce, with only a small number of parameters, several different spacetime geometries, the question of how many expansion orders in each direction are required to accurately describe physical processes within this parametric framework was not addressed in Ref. [14].

However, it is important to establish whether such a framework can reproduce, to high precision, the strong field behavior of geodesics in the vicinity of the event horizon of different black hole spacetimes. Calculating the black hole shadow through direct numerical integration of the geodesic equations in the parametrized form of a reference black hole metric (and repeating the calculation at successive expansion orders), and subsequently comparing this with the shadow obtained from the analytic form of the "unparametrized" metric, provides a practical and stringent test of this framework. In addition, ray-tracing calculations of the shadows cast by different black hole solutions can provide insight into the practical performance of the application of this parametrization in astrophysical calculations involving electromagnetic radiation.

Such a framework has several important applications.

(1) To enable black hole solutions in many metric theories of gravity to actually be written in algebraic form and therefore investigated using ray-tracing and radiative-transfer methods.

(2) To represent all black hole solutions in terms of just a few parameters, distinguishing between solutions on this basis.

(3) To constrain and potentially (physically) exclude black hole solutions from many theories of gravity with just a few key observational parameters necessary to reproduce the shadow curve (see [15] for a general approach).

In this first study we concern ourselves only with the shadow images obtained from black holes in different metric theories of gravity. Since the observed properties of radiation emanating from a black hole are subject to the spacetime through which the radiation propagates, it is prudent to first develop a method to ray trace through a general parametrized metric and investigate the accuracy of this parametrization.

Hence, we here numerically calculate the shadow boundary curve and investigate, for several different spacetimes, the accuracy of the parametrization at various orders with respect to the original unparametrized form of the spacetime. Since the parametrization exactly reproduces Kerr in the equatorial plane, and in order to adequately test the parametrization, we consider near-extremal values of all spacetime-specific deformation parameters. Different measures of the accuracy of the expansion for each spacetime are presented and the excellent convergence properties of the parametrization are demonstrated.

This paper is organized as follows. In Sec. II we describe the ray-tracing formalism required to calculate geodesics within an arbitrary metric parametrization, where the expressions for such calculations are derived explicitly. Section III presents a short overview of the axisymmetric parametrization framework employed throughout this paper. In Sec. IV we apply this ray-tracing formalism to several different known black hole solutions. Each parametrized black hole solution is expanded to various orders and the resultant black hole shadows are calculated and compared with the shadow from the "exact" metric. Finally, Sec. V is devoted to the conclusions.

II. RAY-TRACING FORMALISM

In order to calculate the shadow image of a black hole, one must first solve the geodesic equations in the background spacetime under consideration. For the Kerr spacetime, there now exist several codes and schemes to perform this task (e.g., [16–22]).

As the order of the series expansion of the metric coefficients increases, the expressions for these coefficients grow rapidly in algebraic complexity. Conventional methods to solve the geodesic equations either through quadratures or by directly integrating the geodesic equations are both impractical and inefficient, as well as prone to large numerical errors.

Direct integration of the geodesic equations necessitates determining the Christoffel symbols for the expanded metric at any given order. Given the complexity of the expanded forms, this is impractical and the resultant algebraic expressions can span hundreds of lines of code per Christoffel symbol component. Moreover, such large expressions lead to a catastrophic loss of numerical precision before the ray propagation even begins. A naive approach would be to calculate the Christoffel symbols numerically, but this again is inefficient since when evaluating partial derivatives of the metric coefficients there are many repeated (as well as zero) terms, and the computational overhead is significant. Since we seek to minimize the number of operations needed to integrate the geodesic, we must recast the geodesic equations in a form better suited to satisfy these requirements.

A. Geodesic equations of motion

For a given metric $g_{\alpha\beta}$, the Lagrangian may be written as

$$2\mathcal{L} = g_{\alpha\beta}\dot{x}^{\alpha}\dot{x}^{\beta}, \tag{1}$$

where an overdot denotes differentiation with respect to the affine parameter, λ. Making x^{α} the variable of interest, deriving the Euler-Lagrange equations and solving for $\ddot{x}^{\alpha}$ yields

$$g_{\alpha\beta}\ddot{x}^{\beta} = \partial_{\alpha}\mathcal{L} - \dot{g}_{\alpha\beta}\dot{x}^{\beta}, \tag{2}$$

which may be rewritten, upon raising and relabeling indices, as

$$\ddot{x}^{\alpha} = g^{\alpha\beta}(\partial_{\beta}\mathcal{L} - \dot{g}_{\beta\gamma}\dot{x}^{\gamma}), \tag{3}$$

which are precisely the geodesic equations in a more succinct form.

In solving Eq. (3) numerically, one must also employ the result $d/d\lambda = \dot{x}^{\mu}\partial_{\mu}$ which enables Eq. (3) to be written as

$$\ddot{x}^{\alpha} = g^{\alpha\beta}(\partial_{\beta}\mathcal{L} - \partial_{\mu}g_{\beta\gamma}\dot{x}^{\gamma}\dot{x}^{\mu}). \tag{4}$$

In general, one is only provided with the covariant metric components, perhaps as a series expansion (as in this study), or on a grid of simulation data (which would require interpolation between grid points, e.g., [23]). While one may determine the components of the contravariant metric tensor from an algebraic expression in terms of the determinant of the metric, for general metrics this is cumbersome, computationally expensive and error prone. Instead, we opt for numerical lower-upper decomposition, being careful with singular regions such as those near the event horizon, where the determinant can vanish.

B. Application to axisymmetric spacetimes

Although Eq. (4) represents the geodesic equations for any general metric tensor $g_{\alpha\beta}$, in this study we restrict ourselves to metric expansions of static and axisymmetric spacetimes expressed in Boyer-Lindquist coordinates, where the only off-diagonal metric coefficient is $g_{t\phi}$. As such, Eq. (4) may be rewritten in terms of the following system of second-order ordinary differential equations (ODEs):

$$\bar{g}\ddot{x}^{t} = g_{\phi\phi}\mathcal{T}_{t} - g_{t\phi}\mathcal{T}_{\phi}, \tag{5}$$

$$g_{rr}\ddot{x}^{r} = \partial_{r}\mathcal{L} - \partial_{\mu}g_{rr}\dot{x}^{r}\dot{x}^{\mu}, \tag{6}$$

$$g_{\theta\theta}\ddot{x}^{\theta} = \partial_{\theta}\mathcal{L} - \partial_{\mu}g_{\theta\theta}\dot{x}^{\theta}\dot{x}^{\mu}, \tag{7}$$

$$\bar{g}\ddot{x}^{\phi} = g_{tt}\mathcal{T}_{\phi} - g_{t\phi}\mathcal{T}_{t}, \tag{8}$$

where

$$\mathcal{T}_{t} \equiv \partial_{\mu}g_{tt}\dot{x}^{t}\dot{x}^{\mu}, \tag{9}$$

$$\mathcal{T}_{\phi} \equiv \partial_{\mu}g_{\phi\phi}\dot{x}^{\phi}\dot{x}^{\mu}, \tag{10}$$

and the index μ in Eqs. (5)–(10) ranges from 1 to 2 (i.e., r, θ) only. Additionally, $g \equiv \det(g_{\alpha\beta}) = -g_{rr}g_{\theta\theta}(g_{t\phi}^{2} - g_{tt}g_{\phi\phi})$, where we have also defined

$$\bar{g} \equiv -g(g_{rr}g_{\theta\theta})^{-1} = g_{t\phi}^{2} - g_{tt}g_{\phi\phi}. \tag{11}$$

Solving Eqs. (5)–(8) directly, compared to solving Eq. (4), has the advantage of both removing all vanishing terms and expressing all equations in terms of covariant metric components, thereby simplifying the resulting calculations.[1]

We note that the static and axisymmetric nature of the spacetime implies the conservation of energy, E, and angular momentum, L_{z}, and consequently Eqs. (5) and (8) may be replaced by the following first-order ODEs:

$$\bar{g}\dot{x}^{t} = g_{\phi\phi}E + g_{t\phi}L_{z}, \tag{12}$$

$$-\bar{g}\dot{x}^{\phi} = g_{t\phi}E + g_{tt}L_{z}, \tag{13}$$

where

$$-E = \frac{\partial\mathcal{L}}{\partial\dot{x}^{t}} = g_{tt}\dot{x}^{t} + g_{t\phi}\dot{x}^{\phi}, \tag{14}$$

$$L_{z} = \frac{\partial\mathcal{L}}{\partial\dot{x}^{\phi}} = g_{\phi\phi}\dot{x}^{\phi} + g_{t\phi}\dot{x}^{t}, \tag{15}$$

thereby reducing the number of ODEs to be integrated from 8 to 6.

Two additional constants of motion, namely the particle's rest mass, δ [equal to 0 for photons and -1 for particles in the $(-, +, +, +)$ convention], and the Carter constant, $\mathcal{Q}$, enable the number of ODEs to be further reduced from 6 to 4 [24]. However, Eqs. (6)–(7) are then replaced by first-order ODEs which are of second degree in $\dot{x}^{r}$ and $\dot{x}^{\theta}$, respectively. This introduces ambiguity in the signs of $\dot{x}^{r}$ and $\dot{x}^{\theta}$ at turning points in the geodesic motion due to the presence of square roots in the equations. It is therefore more straightforward to simply integrate Eqs. (6)–(7) and avoid this issue altogether [19].

Although for any static and axisymmetric spacetime the energy and angular momentum of a test point particle are conserved, for the purposes of comparing results at different expansion orders it is more convenient not to enforce that E and L_{z} must be conserved by construction. For the same geodesic calculated at different orders of the

---

[1]In particular, one may exploit the fact that, for axisymmetric spacetimes, the following identities hold: $g^{rr}g_{rr} = g^{\theta\theta}g_{\theta\theta} = 1$, $g^{tt} = -g_{\phi\phi}\bar{g}^{-1}$, $g^{t\phi} = g_{t\phi}\bar{g}^{-1}$, and $g^{\phi\phi} = -g_{tt}\bar{g}^{-1}$.

expansion of the same spacetime, E, L_z and $\dot{x}^t$ are also different at each expansion order.

Furthermore, when considering metrics written in more general (e.g., Cartesian or modified and horizon-penetrating) coordinate systems, it is useful to numerically calculate all components of x^α and $\dot{x}^\alpha$ for practical general-relativistic radiative transfer calculations, e.g., involving general-relativistic magnetohydrodynamical simulation data (e.g. [23]). With x^α and $\dot{x}^\alpha$ fully computed, we calculate the values of $(E, L_z, \delta, \mathcal{Q})$ at every step of the geodesic integration. This enables us to check the accuracy of the integration by monitoring the conservation of these computed constants of motion with respect to their initial values at the beginning of the geodesic integration. For these reasons, in this study we numerically integrate Eqs. (5)–(8) directly.

Partial derivatives are evaluated using finite-difference representations of the differential operators. The background spacetime is always represented algebraically and in closed form in the parametrization scheme so in principle all metric coefficients may be evaluated to machine precision. As such, we find that second-order centered finite differencing with a step size between 10^{-4} and $10^{-5}M$ (where M is the black hole mass) is sufficient for the vast majority of geodesic calculations considered in this paper. Occasionally, switching to a fourth-order method is necessary to maintain numerical precision in problematic regions, e.g., near the event horizon, polar regions or other coordinate-dependent pathologies. In such regions, either forward or backward finite-differencing methods are particularly useful.

Each geodesic is calculated to a precision of better than $10^{-9}M$ using a fourth-order Runge-Kutta-Fehlberg integrator with adaptive step sizing and fifth-order error control [25]. If the input spacetime were, for example, tabulated on a grid, then interpolation between grid points would be required and thus higher order finite-differencing methods would become necessary to preserve accuracy.

C. Initial conditions

As is customary in ray-tracing calculations, an observer needs to be placed at some distance from the source. In our calculations the observer is positioned far from the black hole (i.e., at $r_{\text{obs}} = 10^3 M$), where the spacetime is assumed to be essentially flat. The observer's position is specified in Boyer-Lindquist (oblate spheroidal) coordinates as $(r_{\text{obs}}, \theta_{\text{obs}}, \phi_{\text{obs}})$.

The observer's image plane is a two-dimensional rectangular grid with zero curvature, where each ray arrives perpendicular to the grid. The initial conditions of each ray are then specified by transforming the (x, y) coordinates of the image plane into Boyer-Lindquist coordinates in the black hole frame. The observer's z-direction is oriented along the radial direction towards the black hole center. After this transformation, the coordinates of each pixel on the image plane are expressed as follows:

$$r^2 = \sigma + \sqrt{\sigma^2 + a^2 Z^2}, \tag{16}$$

$$\cos\theta = Z/r, \tag{17}$$

$$\tan\phi = Y/X, \tag{18}$$

where

$$X \equiv \mathcal{D}\cos\phi_{\text{obs}} - x\sin\phi_{\text{obs}}, \tag{19}$$

$$Y \equiv \mathcal{D}\sin\phi_{\text{obs}} + x\cos\phi_{\text{obs}}, \tag{20}$$

$$Z \equiv r_{\text{obs}}\cos\theta_{\text{obs}} + y\sin\theta_{\text{obs}}, \tag{21}$$

and

$$\sigma \equiv (X^2 + Y^2 + Z^2 - a^2)/2, \tag{22}$$

$$\mathcal{D} \equiv \sin\theta_{\text{obs}}\sqrt{r_{\text{obs}}^2 + a^2} - y\cos\theta_{\text{obs}}. \tag{23}$$

The components of the three-velocity of the ray are calculated through differentiation of Eqs. (16)–(18), yielding

$$-\Sigma\dot{x}^r = r\mathcal{R}\sin\theta\sin\theta_{\text{obs}}\cos\Phi + \mathcal{R}^2\cos\theta\cos\theta_{\text{obs}}, \tag{24}$$

$$-\Sigma\dot{x}^\theta = \mathcal{R}\cos\theta\sin\theta_{\text{obs}}\cos\Phi - r\sin\theta\cos\theta_{\text{obs}}, \tag{25}$$

$$\mathcal{R}\dot{x}^\phi = \sin\theta_{\text{obs}}\sin\Phi\,\text{cosec}\theta, \tag{26}$$

where

$$\Sigma \equiv r^2 + a^2\cos^2\theta, \tag{27}$$

$$\mathcal{R} \equiv \sqrt{r^2 + a^2}, \tag{28}$$

$$\Phi \equiv \phi - \phi_{\text{obs}}. \tag{29}$$

Without loss of generality, the initial condition for the time coordinate is set to be $t = 0$ for all rays originating from the observer. The final initial condition for $\dot{x}^t$ is calculated from the invariance of the line element, yielding

$$\dot{x}^t = \beta + \sqrt{\beta^2 + \gamma}, \tag{30}$$

where

$$\beta \equiv -\frac{g_{ti}\dot{x}^i}{g_{tt}}, \tag{31}$$

$$\gamma \equiv \frac{\delta - g_{ij}\dot{x}^i\dot{x}^j}{g_{tt}}. \tag{32}$$

Latin indices $\{i, j\}$ range from 1 to 3 (i.e., r, θ, ϕ) and denote the spatial components.

III. PARAMETRIZATION FRAMEWORK

We present here a brief overview of the parametrization framework used throughout this study. Further details and discussion may be found in Ref. [14]. We recall that in this parametrization, any axisymmetric black hole spacetime with mass M and rotation parameter a can be represented by the following line element [14],

$$ds^2 = -\frac{N^2 - W^2\sin^2\theta}{K^2}dt^2 - 2Wr\sin^2\theta dt d\phi$$
$$+ K^2 r^2 \sin^2\theta d\phi^2 + S\left(\frac{B^2}{N^2}dr^2 + r^2 d\theta^2\right), \quad (33)$$

where

$$S \equiv \frac{\Sigma}{r^2} = 1 + \frac{a^2}{r^2}\cos^2\theta, \quad (34)$$

and N, B, W, K are functions of the radial and polar (expanded in terms of $\cos\theta$) coordinates as follows:

$$B = 1 + \sum_{i=0}^{\infty} B_i(r)(\cos\theta)^i, \quad (35a)$$

$$W = \sum_{i=0}^{\infty} \frac{W_i(r)(\cos\theta)^i}{S}, \quad (35b)$$

$$K^2 = 1 + \frac{aW}{r} + \frac{a^2}{r^2} + \sum_{i=1}^{\infty} \frac{K_i(r)(\cos\theta)^i}{S}, \quad (35c)$$

$$N^2 = \left(1 - \frac{r_0}{r}\right)A_0(r) + \sum_{i=1}^{\infty} A_i(r)(\cos\theta)^i, \quad (35d)$$

where r_0 is the radius of the event horizon in the equatorial plane.[2]

We next expand the coefficients in terms of the radial coordinate as follows,

$$B_i(r) = b_{i0}\frac{r_0}{r} + \tilde{B}_i\frac{r_0^2}{r^2}, \quad (36a)$$

$$W_i(r) = w_{i0}\frac{r_0^2}{r^2} + \tilde{W}_i\frac{r_0^3}{r^3}, \quad (36b)$$

$$K_{i>0}(r) = k_{i0}\frac{r_0^2}{r^2} + \tilde{K}_i\frac{r_0^3}{r^3}, \quad (36c)$$

$$A_0(r) = 1 - \epsilon_0\frac{r_0}{r} + (a_{00} - \epsilon_0)\frac{r_0^2}{r^2} + \frac{a^2}{r^2} + \tilde{A}_0\frac{r_0^3}{r^3},$$

$$A_{i>0}(r) = K_i(r) + \epsilon_i\frac{r_0^2}{r^2} + a_{i0}\frac{r_0^3}{r^3} + \tilde{A}_i\frac{r_0^4}{r^4}, \quad (36d)$$

---

[2]In Ref. [13] the compactified radial coordinate $x \equiv 1 - r_0/r$ was introduced to simplify the expressions; while we could use such a coordinate here as well, we resort to the radial coordinate r to ease the comparison with the original unparametrized metrics.

where the tilded functions are given by

$$\tilde{B}_i \equiv \frac{b_{i1}}{1 + \frac{b_{i2}(1-\frac{r_0}{r})}{1+\frac{b_{i3}(1-\frac{r_0}{r})}{1+\dots}}}, \quad (37a)$$

$$\tilde{W}_i \equiv \frac{w_{i1}}{1 + \frac{w_{i2}(1-\frac{r_0}{r})}{1+\frac{w_{i3}(1-\frac{r_0}{r})}{1+\dots}}}, \quad (37b)$$

$$\tilde{K}_i \equiv \frac{k_{i1}}{1 + \frac{k_{i2}(1-\frac{r_0}{r})}{1+\frac{k_{i3}(1-\frac{r_0}{r})}{1+\dots}}}, \quad (37c)$$

$$\tilde{A}_i \equiv \frac{a_{i1}}{1 + \frac{a_{i2}(1-\frac{r_0}{r})}{1+\frac{a_{i3}(1-\frac{r_0}{r})}{1+\dots}}}. \quad (37d)$$

Any approximation given by the above form of the metric is characterized by two orders: the order of expansion in $\cos\theta$ (m) and the order of the radial expansion (n). Specifying a finite number m means discarding all higher orders of the expansion, i.e., we set $B_{i>m} = 0$, $W_{i>m} = 0$, $K_{i>m} = 0$ and $A_{i>m} = 0$. As noted in [14], it is not always possible to choose $a_{ij} = 0$, for any given $j > 1$, in a consistent manner. The same applies to the other continued-fraction coefficients, b_{ij}, w_{ij}, and k_{ij}. This is why, in some cases, not all of the coefficients in the radial expansion of order n vanish for $j > n$, but their exact values are substituted only for $j \leq n$.

IV. TESTING THE PARAMETRIZATION WITH SHADOW CALCULATIONS

Unless stated explicitly otherwise, hereafter the observer is positioned at $i \equiv \theta_{\text{obs}} = \pi/2$, i.e., in the equatorial plane of a rotating black hole. This provides the most extreme test of the effects of gravitational lensing on the size and shape of the shadow image. In calculating each shadow, due to the top-bottom symmetry of the image one need only calculate the upper half of the shadow and simply reflect this in the observer's x axis.

Consider the left panel of Fig. 1. A black hole shadow may be represented as a closed parametric curve of radius $\rho(\psi)$, where $\psi = [0, \pi]$, since the shadow is symmetric about the x axis. The interval ψ is divided into 10^3 equally spaced points, and for each value of ψ bisection is performed along ρ until convergence with the shadow boundary is reached. Since the shadow is a single closed curve and ψ is fixed, the bisection is one dimensional and always around a single unknown but real and bounded point.

The bisection begins with the inner boundary placed at $(\alpha, \beta) = (0, 0)$ and the outer boundary placed at the outermost (α, β) value for the particular value of ψ chosen, e.g., for Fig. 1, when choosing $\psi = 45°$ the inner and outer boundaries are placed at $(0, 0)$ and $(8, 8)$, respectively. At both points a ray is fired towards the black hole and whether each ray is captured by the black hole (interior to the shadow) or escapes to infinity (exterior to the shadow) is determined. Convergence is then defined as when the
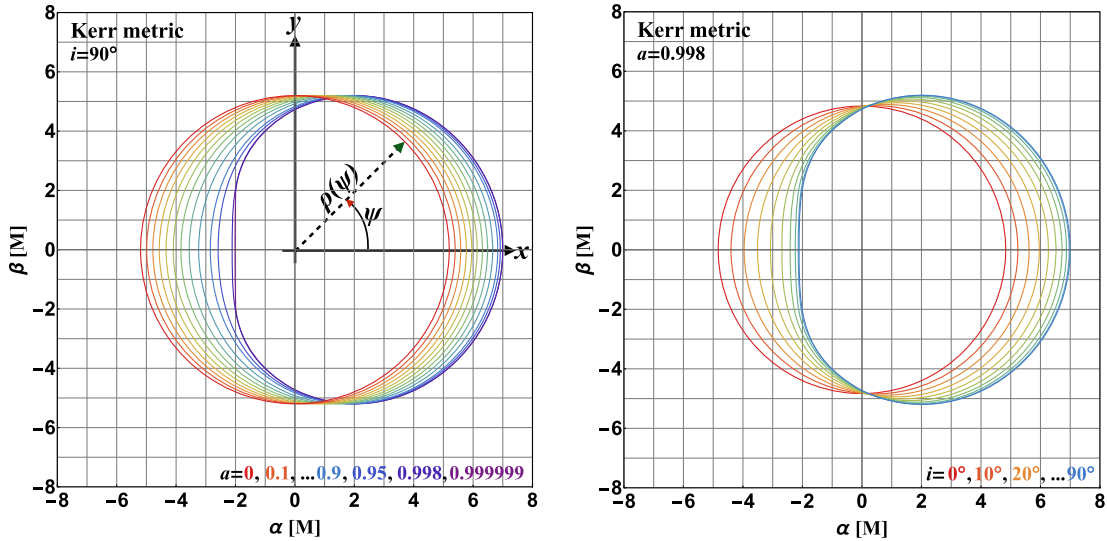
FIG. 1.   Shadows cast by a Kerr black hole. Left panel: As viewed by an observer at $i \equiv \theta_{\rm obs} = 90°$, with black hole spin parameters varied as 0 (red, leftmost), $0.1, 0.2, \ldots, 0.9, 0.95, 0.998$ and $1 - 10^{-6}$ (purple, rightmost). Right panel: Spin parameter fixed as $a = 0.998$ and i varied as 0° (red, leftmost), $10°, 20°, \ldots, 90°$ (blue, rightmost).

rays are within $10^{-6}M$ of the shadow boundary, i.e., bisection continues until the bisection step size is smaller than $10^{-6}M$.

Before calculating shadows from more complicated expansions of metrics, it is instructive to consider first the shadow from a Kerr black hole, whose line element may be written in Boyer-Lindquist coordinates as

$$ds^2 = -\left(1 - \frac{2Mr}{\Sigma}\right)dt^2 + \frac{\Sigma}{\Delta}dr^2 + \Sigma d\theta^2$$
$$- \frac{4aMr\sin^2\theta}{\Sigma}dtd\phi + \frac{\mathcal{A}\sin^2\theta}{\Sigma}d\phi^2, \qquad (38)$$

where

$$\Delta \equiv r^2 - 2Mr + a^2, \qquad (39)$$

$$\mathcal{A} \equiv \Sigma\Delta + 2Mr(r^2 + a^2). \qquad (40)$$

Figure 1 presents shadows cast by a Kerr black hole for a fixed observer position and varying spin parameter (left panel) and for a fixed extremal spin parameter and varying observer inclination angle (right panel). It can be seen that increasing the black hole spin shifts the shadow image to the right, rendering it more asymmetric and sharpening the deviation from a circular shape, while the vertical extent of the shadow remains unchanged (right panel). Fixing instead the spin parameter to $a = 0.998$ and varying the observer inclination angle both shifts the shadow and increases its vertical extent (left panel).

The parametrization employed in this study exactly reproduces the Kerr metric in the equatorial plane. Consequently, a stringent test of the convergence properties of this parametrization is best performed when considering

large values of the deformation parameters of the parametrized metric. While such large parameters may not be physically realistic, they represent an important and practical "stress test" of the parametrization of each metric at different expansion orders in the radial and polar coordinates.

A. General testing setup

As discussed in [14], the axisymmetric expansion of the metric may be in terms of r (radial coordinate), $\cos\theta$ (where θ is the polar coordinate) or a combination of the two. It is important to remember that all axisymmetric black holes considered in this study possess mirror symmetry, meaning that only even powers of $\cos\theta$ are nonzero in the expansion. In this study, three distinct black hole metrics are considered, each being represented as a series expansion. The first is the Kerr-Sen metric [26], where an exclusively radial expansion is employed. The second is the Einstein-dilaton-Gauss-Bonnet (EDGB) [11] metric, which we expand in terms of $\cos\theta$, leaving the coefficients in their exact form as functions of the radial coordinate. The third metric is that proposed by Johannsen and Psaltis [28], wherein the expansion is performed in both the radial coordinate and in $\cos\theta$.

In order to validate, both qualitatively and quantitatively, the convergence properties and behavior of the metric expansion, several tests are performed. Naturally, given the original expression for a metric and its series expansion at any particular order, one may visually compare the shadow calculated from both forms of the metric, providing a qualitative view of the performance of the expansion. This is the first test, whereby the shadow calculated from the original metric is plotted in black, and the shadows

obtained from the expansion of this metric at successive orders are overplotted as colored curves for comparison.

As it can be seen in Fig. 1 (left panel), the shadow may be represented as a closed parametric curve $\rho(\psi)$. In calculating the shadow a bisection scheme is employed and the $\rho(\psi)$ value for each sampled ψ is recorded. The value of $\rho(\psi)$ is calculated both for the original metric and for the various orders of expansion of this metric. From this, the percentage error difference between the original metric and any given order of the same expanded metric, i.e., $100 \times |1 - \rho(\psi)_{\text{analytic}}/\rho(\psi)_{\text{expanded}}|$, may be calculated as a function of ψ along the shadow boundary. Since $\psi = [0, \pi]$, the percentage error is plotted as a function of $\cos\psi = [-1, 1]$. This constitutes the second test.

Since each shadow is a closed parametric curve, and given that only the upper half of the shadow needs to be calculated, another measure of the accuracy of the expansion is the area of the half shadow. Since we store the (x, y) coordinates of the shadow boundary curve we readily obtain the area by calculating $\int_{x_{\text{min}}}^{x_{\text{max}}} dx\, y(x)$ numerically. Finally, the third test of the expansion is the percentage error difference between the half-shadow areas of the original metric and its corresponding expansion.

B. Kerr-Sen metric

An exact solution of the equations of motion corresponding to the low-energy effective field approach of the heterotic string theory was found by Sen in Ref. [26]. This solution describes a charged, axially symmetric black hole (the Kerr-Sen black hole) [26,27], whose charge also introduces the presence of a scalar (dilaton) field b. The Kerr-Sen (Sen) metric is a particular case of a more general axion-dilaton black hole with a null Newman-Unti-Tamburino charge [29], and it can be described by the line element (33) if one chooses the expansion in [14], yielding

$$W = \frac{2a(\mu + b)(\sqrt{r^2 + b^2} - b)}{r(r^2 + a^2\cos^2\theta)}, \tag{41a}$$

$$B^2 = \frac{r^2}{b^2 + r^2}, \tag{41b}$$

$$K^2 = \left(1 + \frac{a^2\cos^2\theta}{r^2}\right)^{-1}\left[\left(1 + \frac{a^2}{r^2}\right)^2 - \frac{a^2\sin^2\theta}{r^2}N^2\right], \tag{41c}$$

$$N^2 = \frac{(\sqrt{b^2 + r^2} - b)^2 - 2\mu(\sqrt{b^2 + r^2} - b) + a^2}{r^2}, \tag{41d}$$

where the Arnowitt-Deser-Misner mass is now given by $M = \mu + b$. Hereafter we measure the parameters a and b in units of μ, i.e., we choose $\mu = 1$.

The radial expansion of the Kerr-Sen metric is calculated from the first through the fourth order. The results of

ray-tracing calculations of the shadows from the radial expansion for the Kerr-Sen metric are illustrated in the left panels of Figs. 2 and 3 for values of the dilaton field given by $b = 0.5$ and $b = 1$, respectively.

In the left panels of Fig. 2, the first-order expansion (blue line) and the second-order expansion (red line) are still visible and most distinct from the exact shadow boundary (black line) towards the left half of the image. For the right half of the image, on the other hand, the agreement is excellent and improves as the shadow traverses the equatorial plane ($y = 0$ in the shadow image). The third- and fourth-order expansions (orange and green lines, respectively) cannot be seen and overlay the exact black curve very well. As expected, the effect of increasing the spin parameter from 0.9 to 0.998 is to further distort the shadow image and slightly slow the convergence, as evidenced by the blue and red curves being visually further apart from the black curve in the $a = 0.998$ case.

In the right panels of Fig. 2 we show instead the relative error (as a percentage) of each expansion order of the Kerr-Sen metric relative to the exact metric; the various curves are plotted as a function of ψ along the shadow boundary. For $a = 0.95$, the maximum error in the first-order expansion (blue line) is $\sim$1.7%. At second order (blue line) this drops to $\sim$0.25% and by the third (orange line) and fourth order (green line) the error is negligible and thus the orange and green curves appear as horizontal lines.

As an additional stress test of the parametrization approach, we consider in Fig. 3 the more extreme deformations which follow when considering a dilaton field with $b = 1$. We note that the effect of increasing b is that of increasing the absolute size of the shadow (the mass is proportional to b), so that the error inherent to each expansion order also increases. Overall, the behavior shown in Fig. 3 is very similar to that of Fig. 2, with the second and higher order radial expansions again exhibiting excellent convergence properties. Furthermore, and as found for lower values of b, the error plots demonstrate that already at the second order the error is everywhere below 0.3% and that the error at third and fourth order is very close to 0 across the entire shadow.

As a final check of the accuracy and convergence of the series expansion, the half-shadow area (i.e., for $\psi \in [0, \pi/2]$) for both the exact Kerr-Sen metric and its four different expansion orders is calculated. These results are presented in Table I, where four different values of the black hole spin parameter (i.e., $a = 0.2, 0.5, 0.95, 0.998$) are considered both for $b = 0.5$ and for $b = 1$. The table also reports as $\epsilon_{n,m}$ the relative error between the area computed from the exact metric shadow and that obtained from the same expanded metric shadow at order n in the radial direction and m in the polar direction.

In the case of slowly rotating black holes, i.e., $a = 0.2$, the error in the area for the first-order expansion is
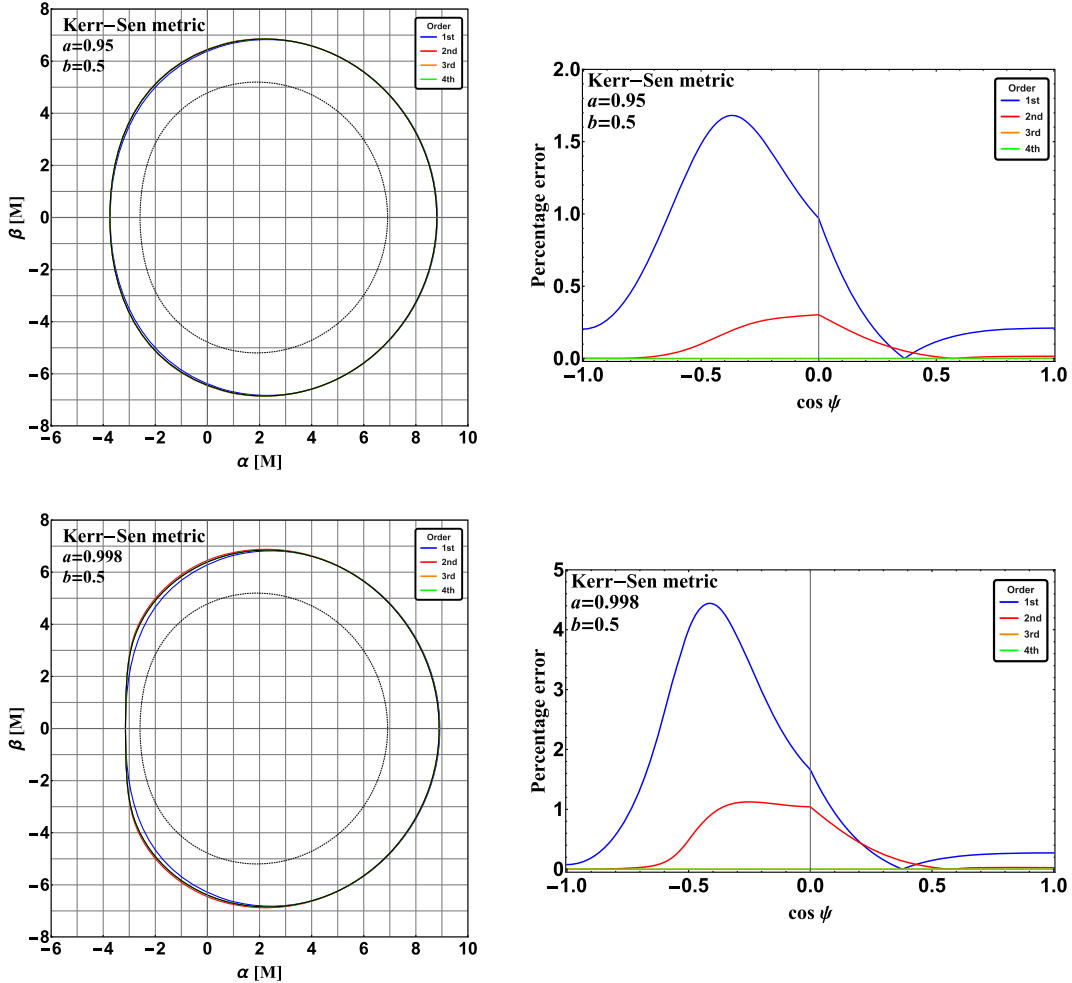
FIG. 2.   Left column: Shadows from the *radial* expansion of the Kerr-Sen metric for $b = 0.5$ as viewed by an observer in the equatorial plane of the black hole for $a = 0.95$ (top) and $a = 0.998$ (bottom). The black curve represents the exact analytic form of the metric. Blue (first order), red (second order), orange (third order) and green (fourth order) curves represent the radial metric expansion. For comparison, the dotted curve shows the shadow from a Kerr black hole with the same spin parameter. Right column: Corresponding percentage error plots of each expansion order with respect to the original Kerr-Sen metric as a function of $\cos \psi$ along the shadow boundary curve.

$\sim 10^{-4}\%$ and by the fourth-order expansion it is within the precision used to calculate the shadow and thus effectively 0. This trend also holds for $a = 0.5$ (moderate spin), which is why shadow and error plots for these values were not presented. For higher spins, the error at first order is larger but still at the one percent level. More importantly, it can be seen that the values of the area of the shadow rapidly converge to the "true" shadow area as the order of the expansion is increased.

Before concluding this section dedicated to Kerr-Sen black holes we note that the values chosen here both for the spin and for the dilaton field are extreme and likely to be much larger than what would be found for an astrophysical black hole. That being said, the convergence of the radial expansion of the Kerr-Sen metric is both fast and highly accurate even in these extremal cases.

C. Einstein-dilaton-Gauss-Bonnet metric

In $D > 4$ spacetimes, where D is the number of spacetime dimensions, the second-order term in curvature, i.e., the Gauss-Bonnet term, is the dominant one. However, in four-dimensional spacetimes, like those considered in this paper, the Gauss-Bonnet term alone is invariant and leads to solutions of the Einstein equations which are not affected unless the scalar field (dilaton) is coupled to the system. An approximate metric for a rotating black hole in this system with such a dilaton coupling, i.e., in EDGB theory, was deduced in the regime of slow rotation [11]. The metric was obtained in the form of an expansion in terms of two small parameters: ζ and $\chi \equiv a/M$. For finite values of these parameters, the metric has a divergence at the Schwarzschild horizon $r = 2M$. However, the equivalent form proposed in Ref. [14] removes this divergence and the line element then reads
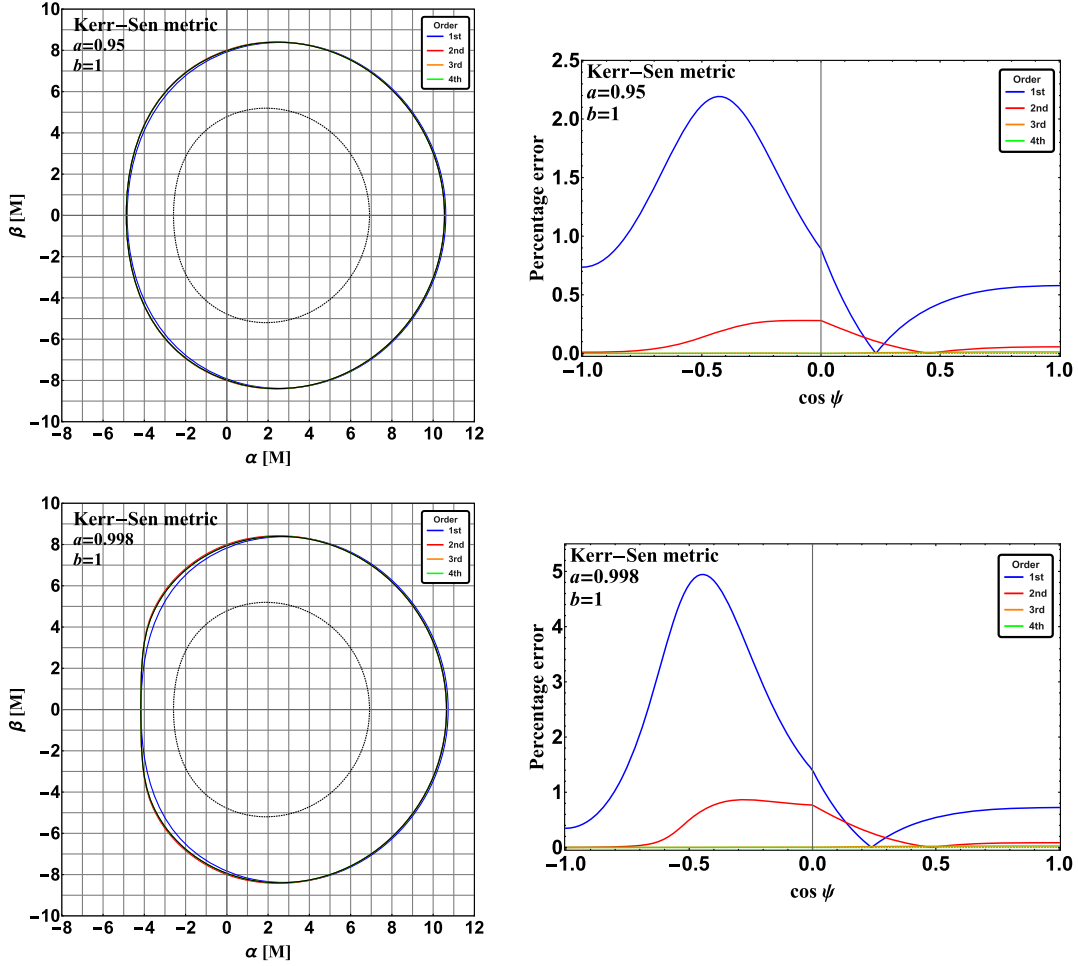
FIG. 3. As in Fig. 2, but now the deformation parameter $b = 1$.

$$ds^2 = -\frac{f - w^2\sin^2\vartheta}{\kappa^2}dt^2 + \frac{\beta^2\sigma}{f}d\rho^2 + \rho^2\sigma d\vartheta^2$$
$$- 2w\rho\sin^2\vartheta dt d\phi + \rho^2\kappa^2\sin^2\vartheta d\phi^2, \quad (42)$$

where the various terms in the metric are given by

$$\kappa^2 = 1 + \chi^2\frac{M^2}{\rho^2}\left[1 + \frac{2M}{\rho}(1 - \cos^2\vartheta)\right]$$
$$+ \zeta\chi^2(\cos^2\vartheta - 1/3)\frac{M^3}{\rho^3}\sum_{k=0}^{7}c_k\frac{M^k}{\rho^k}, \quad (43a)$$

TABLE I. Table of the half-shadow area, $A_{n,m}$ (in units of M^2), and its corresponding percentage error (with respect to the analytic Kerr-Sen metric), $\epsilon_{n,m}$, of each expansion order $\{n,m\}$ of the Kerr-Sen metric. Indices n and m correspond, respectively, to the order of the *radial* and $\cos\theta$ expansions. The exact area obtained from the analytic metric is denoted by A_{exact}. Numbers within square brackets denote multiplicative powers of 10. For the Kerr-Sen metric $\cos\theta$ is fixed at second order and the radial expansion is varied up to fourth order.

a	b	A_{exact}	$A_{1,2}$	$A_{2,2}$	$A_{3,2}$	$A_{4,2}$	$\epsilon_{1,2}$	$\epsilon_{2,2}$	$\epsilon_{3,2}$	$\epsilon_{4,2}$
0.2	0.5	73.5640	73.5641	73.5642	73.5640	73.5640	1.06[−4]	3.22[−4]	3.08[−5]	4.85[−6]
	1.0	110.576	110.601	110.581	110.575	110.576	2.32[−2]	4.38[−3]	4.29[−4]	2.75[−6]
0.5	0.5	72.6472	72.6289	72.6478	72.6471	72.6472	2.52[−2]	8.20[−4]	1.29[−4]	8.18[−6]
	1.0	109.237	109.241	109.240	109.235	109.237	3.83[−3]	2.91[−3]	1.28[−3]	6.11[−5]
0.95	0.5	68.3328	67.9290	68.4379	68.3317	68.3328	5.91[−1]	1.54[−1]	1.49[−3]	1.10[−4]
	1.0	102.953	102.512	103.081	102.940	102.954	4.28[−1]	1.25[−1]	1.25[−2]	9.51[−4]
0.998	0.5	66.7159	65.8826	67.1017	66.7136	66.7160	1.25[+0]	5.78[−1]	3.41[−3]	1.90[−4]
	1.0	100.620	99.7024	101.032	100.588	100.622	9.12[−1]	4.10[−1]	3.13[−2]	1.77[−3]

TABLE II.   Table of coefficients for the nondivergent EDGB metric.

k	c_k	w_k	$f_{k,1}$	$f_{k,2}$	$f_{k,3}$	$\beta_{k,1}$	$\beta_{k,2}$	$\beta_{k,3}$
0	$-4463/875$	-9	$3019/875$	$-3048/875$	$26/3$	2	5	-14
1	$-2074/175$	-140	$11201/1750$	$-18551/5250$	$22/5$	11	$139/15$	$-128/5$
2	$-266911/12250$	-90	$-1497089/36750$	$838039/110250$	$32/5$	$2767/15$	$-907/45$	-48
3	$-12673/525$	-144	$30316/3675$	$-253756/11025$	$-80/3$	$-208/5$	$616/5$	0
4	$12371/245$	400	$-26233/245$	$1917/245$	0	$1658/5$	$2102/15$	0
5	$3254/35$	...	$9214/21$	$-20422/315$	0	$-26288/15$	$28688/45$	0
6	$2536/15$	...	$-6136/15$	$7336/45$	0	2160	-720	0
7	-240	...	240	-80	0	...	...	...

$$\sigma = 1 + \chi^2 \frac{M^2}{\rho^2}\cos^2\vartheta + \zeta\chi^2(\cos^2\vartheta - 1/3)\frac{M^3}{\rho^3}\sum_{k=0}^{7} c_k \frac{M^k}{\rho^k},$$

$$(43b)$$

$$w = 2\chi \frac{M^2}{\rho^2} + \frac{1}{15}\zeta\chi \frac{M^4}{\rho^4}\sum_{k=0}^{4} w_k \frac{M^k}{\rho^k},$$

$$(43c)$$

$$f = 1 - \frac{2M}{\rho} + \chi^2 \frac{M^2}{\rho^2} + \zeta\frac{M^3}{6\rho^3}(2-\chi^2)$$
$$+ \zeta\frac{M^4}{\rho^4}\sum_{k=0}^{7}(\chi^2\cos^2\vartheta f_{k,1} + \chi^2 f_{k,2} + f_{k,3})\frac{M^k}{\rho^k},$$

$$(43d)$$

$$\beta^2 = 1 + \frac{M^2}{6\rho^2}(\chi^2-2)\left(3+\frac{8M}{\rho}\right)$$
$$+ \zeta\frac{M^4}{\rho^4}\sum_{k=0}^{6}(\chi^2\cos^2\vartheta \beta_{k,1} + \chi^2 \beta_{k,2} + \beta_{k,3})\frac{M^k}{\rho^k}.$$

$$(43e)$$

The numerical values for the coefficients in the series in Eqs. (43) may be found in Table II.

In order to transform this metric into the form of Eq. (33) we proceed as in Ref. [14]. We rewrite Eq. (42) in the form (33) by imposing that in terms of the new coordinates, r and θ, relation (34) and the additional condition

$$\left(K^2 - 1 - \frac{aW}{r} - \frac{a^2}{r^2}\right)\Bigg|_{\theta=\frac{\pi}{2}} = 0$$

are fulfilled. Finally, we obtain the functions B, W, K^2, and N^2 as an infinite series in terms of $\cos\theta$, as in (35). The lowest order is then given by expressions (80) in Ref. [14], which we do not report here for compactness. To provide a test of the polar expansion, the nondivergent EDGB metric is expanded up to eighth order in powers of $\cos\theta$. This is then compared with the exact form of the nondivergent EDGB metric given in Eq. (42).

Figure 4 presents shadow calculations for the EDGB metric at successive expansion orders in $\cos\theta$. The spin parameter is chosen as $a = 0.5$, which is near the limit of validity of the EDGB solution, itself only derived in the

literature for very small values of the spin parameter. Two values of the deformation parameter, ζ, are chosen as 0.1 and 0.15. We recall that the value $\zeta = 0.15$ is a critical value, beyond which, for $a = 0.5$, the EDGB metric would develop a naked singularity. As such, these deformation parameters coupled with the moderate spin parameter represent an extreme test of the behavior of the metric expansion.

As it can be seen in the top row of Fig. 4, near the equatorial plane, and for the majority of the region away from the poles, the expansion at all orders is in close agreement with the exact EDGB metric. However, considering the $\alpha < 0$ portion of the shadow, the shadow in the expanded metric begins to differ more significantly from the analytic one when approaching the polar region, before reconverging towards precisely $\theta = \pi/2$. This behavior is then mirrored in the $\alpha > 0$ portion of the shadow.

To see this more clearly, a magnified view of the neighborhood of the polar region is presented in the middle row of Fig. 4. The expansion exhibits some mild oscillatory behavior as it approaches the pole, diminishing as the order of the expansion is increased. The red (fourth order and second order in $\cos^2\theta$) and orange (sixth order and third order in $\cos^2\theta$) curves are almost indistinguishable in this region, but upon closer inspection of the image, the red curve is always above the orange curve. The small discrepancy observed in the polar region is not due to any singular behavior in the expansion of the EDGB metric itself, but merely a reflection of the fact that the expansion is made near the equatorial plane and, in this instance, yields the largest error near the poles.

The bottom row of Fig. 4 reports the percentage relative error and, as expected, it demonstrates that the expansion worsens near the pole and the error may be as large as 14% in the case of the second-order expansion. However, in this instance a global measure of the shadow, namely the half-shadow area, is perhaps more representative of the overall performance. Table III shows that for $\zeta = 0.1$ the error is always less than 1%. The effect of increasing the value of ζ is to decrease the radius of the event horizon, and therefore the photon region and by extension the calculated area of the half shadow. For $\zeta = 0.15$ the error is 1.45%. In both cases the convergence of the expansion as the order is increased is clear.
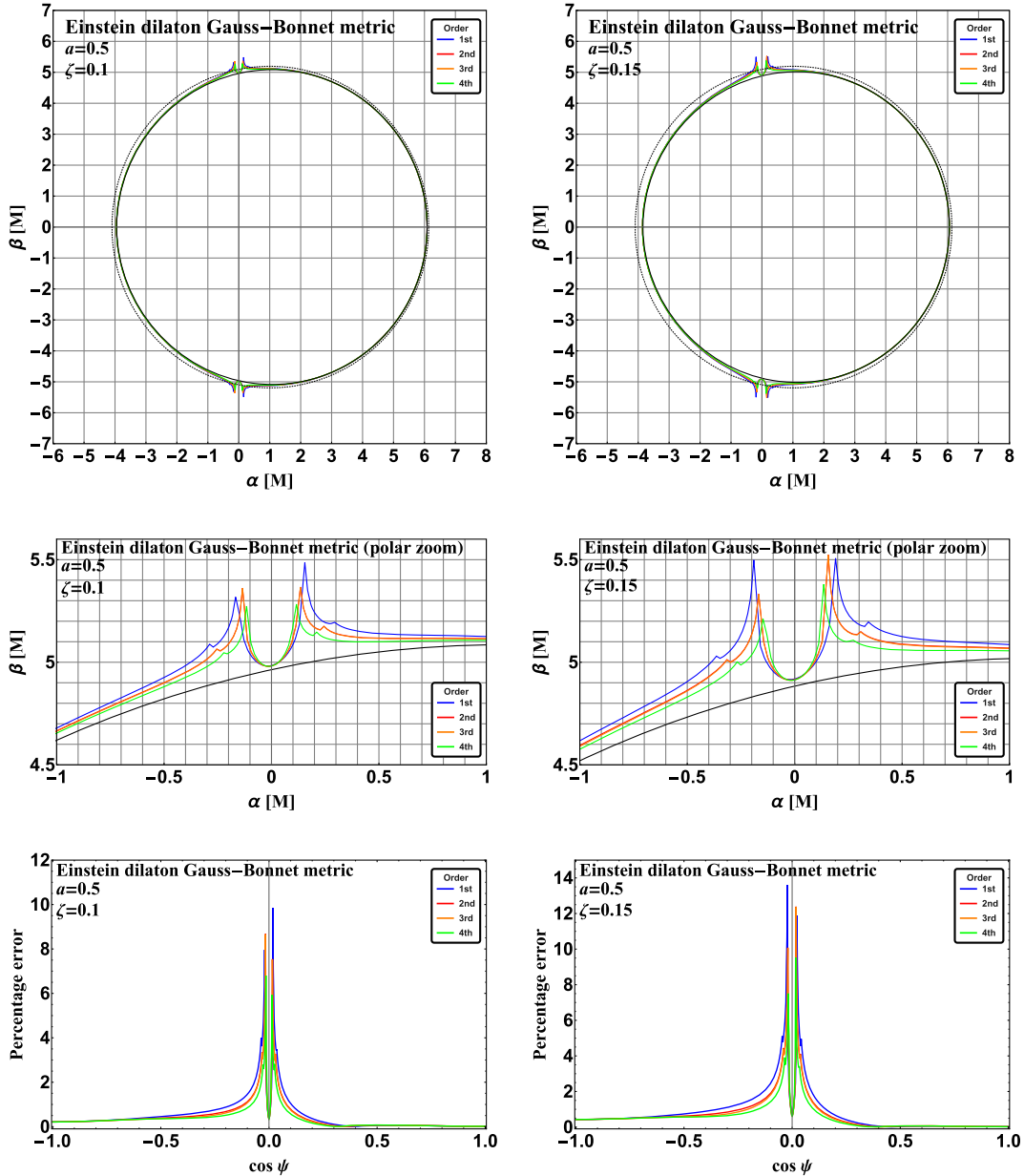
FIG. 4.   Top row: Shadows from the polar coordinate expansion of the EDGB metric with spin parameter $a = 0.5$ for deformation parameters $\zeta = 0.1$ (left panel) and $\zeta = 0.15$ (right panel). Middle row: A magnified view of the polar region. Bottom row: Percentage error plots of each expansion order relative to the original EDGB metric. Blue, red, orange and green curves denote the expansion at first, second, third and fourth order in $\cos^2 \theta$, respectively. For comparison, the dotted curve shows the shadow from a Kerr black hole with the same spin parameter.

At this point it is important to emphasize that the EDGB metric discussed above is essentially non-Kerr in the sense that it refers to a non-Einsteinian theory of gravity built out of the Einstein-Hilbert action and of a scalar field coupled to the higher curvature Gauss-Bonnet term. Furthermore, the values of the coupling constants χ and ζ are chosen in the test to be rather large so as to produce a smooth but non-negligible deformation of the spacetime geometry. In this respect, the EDGB metric represents not only a very good (and challenging) test for the parametrization

approach, but also a demanding benchmark for the new ray-tracing formalism.

D. Johannsen-Psaltis metric

As a final test of the metric parametrization we consider the Johannsen-Psaltis metric [28], where, for simplicity, we take ε_3 as the only nonzero deformation parameter. In this case, the Johannsen-Psaltis metric may be written as

TABLE III.   Table of half-shadow areas and their corresponding percentage errors for the first four successive expansion orders of the EDGB metric. The expansion considered in this case is in terms of $\cos^2\theta$ only.

a	ζ	A_{exact}	$A_{0,2}$	$A_{0,4}$	$A_{0,6}$	$A_{0,8}$	$\epsilon_{0,2}$	$\epsilon_{0,4}$	$\epsilon_{0,6}$	$\epsilon_{0,8}$
0.5	0.1	39.9885	40.3445	40.2700	40.2559	40.2088	8.90[−1]	7.04[−1]	6.69[−1]	5.51[−1]
	0.15	38.9264	39.4915	39.3773	39.3536	39.2825	1.45[+0]	1.16[+0]	1.10[+0]	9.15[−1]

$$ds^2 = -\frac{f - w^2\sin^2\vartheta}{\kappa^2} dt^2 + \frac{\beta^2\sigma}{f} d\rho^2 + \rho^2\sigma d\vartheta^2$$
$$- 2w\rho\sin^2\vartheta\, dt d\phi + \rho^2\kappa^2\sin^2\vartheta d\phi^2, \qquad (44)$$

where

$$\sigma = 1 + \frac{a^2}{\rho^2}\cos^2\vartheta, \qquad (45a)$$

$$\kappa^2 = \frac{(\rho^2 + a^2)^2 - a^2\sin^2\vartheta(\rho^2 - 2M\rho + a^2)}{\rho^4\sigma}$$
$$+ h\frac{a^2\sin^2\vartheta(\rho^2 + 2M\rho + a^2\cos^2\vartheta)}{\rho^4\sigma}, \qquad (45b)$$

$$\beta = 1 + h, \qquad (45c)$$

$$f = (1 + h)\frac{\rho^2 - 2M\rho + a^2 + a^2h\sin^2\vartheta}{\rho^2}, \qquad (45d)$$

$$w = \frac{2aM(1 + h)}{\rho^2\sigma}, \qquad (45e)$$

$$h = \varepsilon_3\frac{M^3}{\rho^3\sigma^2}. \qquad (45f)$$

Following Ref. [14], we obtain the new coordinates as a series expansion in terms of $\cos^2\vartheta$ as

$$\cos\theta = \left(1 + \varepsilon_3\frac{a^2M^3}{\rho^5}\right)^{-1/2}\cos\vartheta + \mathcal{O}(\cos^3\vartheta), \qquad (46)$$

$$r = \rho\left(1 + \varepsilon_3\frac{a^2M^3}{\rho^5}\right)^{1/2} + \mathcal{O}(\cos^2\vartheta). \qquad (47)$$

Although this series expansion cannot be inverted analytically, one may calculate as many coefficients in the double expansion as is necessary. More specifically, the radial expansion has been considered from the first through the eighth order, while the polar expansion was kept fixed at fourth order in $\cos\theta$. Figure 5 (left column) presents shadows of the first four orders of the expanded form of the Johannsen-Psaltis metric (red, blue, green and orange lines), along with the shadow computed from the analytic metric, which is shown for comparison (black line). As in the previous figures, the right column displays the corresponding relative errors of each shadow as a function of the polar angle ψ.

We have here considered a value $\varepsilon_3 = 0.24$ as this enables the deformations in both the spin and ε_3 to be large. Increasing ε_3 further (without creating a naked singularity) would require decreasing the spin parameter.

Since the metric expansion reproduces Kerr exactly in the equatorial plane and is increasingly accurate for decreasing values of a, and since for fixed spin parameter, increasing ε_3 has the effect of decreasing the shadow size, the aforementioned choice of $\varepsilon_3 = 0.24$ proves useful when scrutinizing the performance of the expansion.

It is clear from the top right panel of Fig. 5, which refers to $\varepsilon_3 = 0.24$, that the series expansion converges more slowly, with the second-order expansion error (red) proving worse than that at first order for approximately $-0.85 \leq \cos\psi \leq 0.15$, i.e., roughly half of the shadow boundary. Similar behavior is also observed for the third-order (orange) and fourth-order (green) curves. This behavior continues for the fifth through eighth orders (not shown in the figure for clarity). However, when considering the half-shadow areas in Table IV the convergence is apparent, except for the $\{6, 4\}$ expansion, for which we find in Table V that $\epsilon_{6,4} > \epsilon_{5,4}$. For this reason the expansion was continued up to eighth order.

Decreasing the value of ε_3 to $\varepsilon_3 = -0.5$, the shadow area grows and this is shown in the left panel of the middle row of Fig. 5. Note that the first-order expansion is now the least accurate, as one would expect (although more accurate that for $\varepsilon_3 = 0.24$). However, inspecting the corresponding right panel for the percentage error reveals that the second-order expansion is, in the region roughly $-0.75 \leq \cos\psi \leq 0.15$, more accurate than both the third- and fourth-order expansions. For $\varepsilon_3 = -1$ this trend continues and it is hard to discern just by looking at the first four expansion orders whether convergence is present.

To address this issue and clarify matters, Tables IV and V report, respectively, the half-shadow areas and their corresponding percentage errors as they are calculated up to the eighth order in the radial coordinate and at second order in $\cos\theta$. While the shadow curves are calculated for all orders, they are only displayed up to fourth order in Fig. 5 since they are visually indistinguishable from the fourth-order case. In this way it is evident upon inspecting Table V that the expansion is indeed convergent. For all values of ε_3 it is found that $\epsilon_{8,4} < \epsilon_{8,2}$, and thus the expansion is convergent.

Two remarks should be made at this point. First, to appreciate the oscillatory behavior in the convergence of the shadow one should recall that parametrization is the result of a *double* expansion in the r and θ directions and that the convergence in each direction occurs at a different "rate." Therefore, it is perfectly possible at some order n of the expansion in one direction and order m in the other
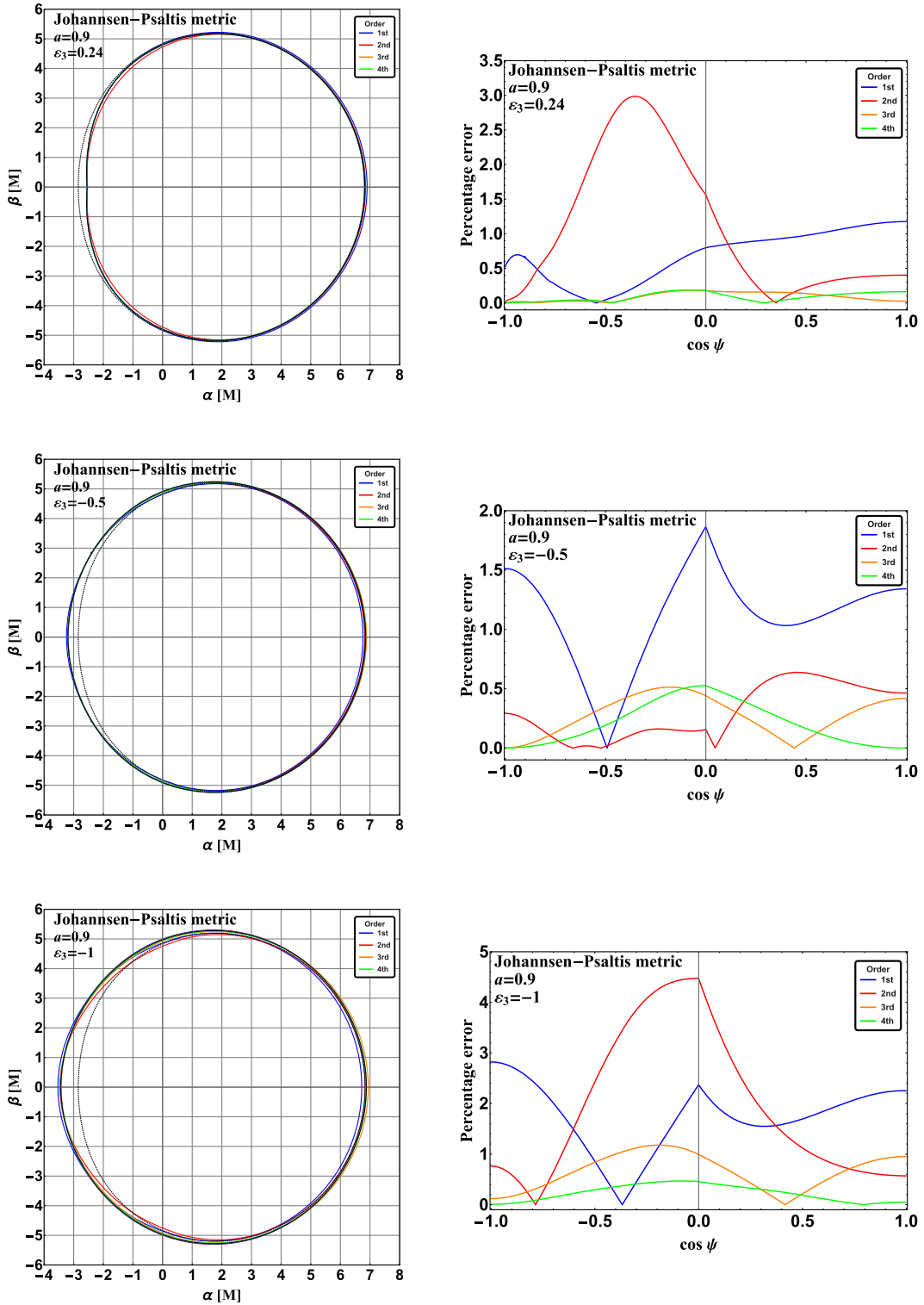
FIG. 5.   Left column: Shadows from the radial expansion of the Johannsen-Psaltis metric with spin parameter $a = 0.9$ for $\varepsilon_3 = 0.24$ (top), $\varepsilon_3 = -0.5$ (middle) and $\varepsilon_3 = -1$ (bottom). Only the first four orders of the expansion are shown. Right column: Percentage errors of each expansion order relative to the original Johannsen-Psaltis metric. Blue, red, orange and green curves denote the expansion at first, second, third and fourth order in $\cos^2 \theta$, respectively. For comparison, the dotted curve shows the shadow from a Kerr black hole with the same spin parameter.

TABLE IV.   Table of half-shadow areas for successive expansion orders of the Johannsen-Psaltis metric. The expansion is fixed at fourth order for $\cos\theta$ whilst the *radial* expansion is considered up to eighth order. Note that for the eighth order radial expansion the value of $A_{8,2}$ (i.e., second order in $\cos\theta$) is included to compare with $A_{8,4}$.

a	ε_3	A_{exact}	$A_{1,4}$	$A_{2,4}$	$A_{3,4}$	$A_{4,4}$	$A_{5,4}$	$A_{6,4}$	$A_{7,4}$	$A_{8,2}$	$A_{8,4}$
	0.24	38.8979	39.5424	38.5721	38.9766	38.8723	38.9158	38.9175	38.8838	38.9171	38.8888
0.9	−0.5	41.2918	40.4947	41.0235	41.2720	41.1276	41.3215	41.3076	41.2778	41.2747	41.2880
	−1.0	42.5892	41.5207	41.1449	42.5444	42.4225	42.6546	42.5539	42.5356	42.5678	42.5806

TABLE V.   Table of percentage errors corresponding to the half-shadow areas for successive expansion orders of the Johannsen-Psaltis metric as reported in Table V. As expected, $\epsilon_{8,4} < \epsilon_{8,2}$ for all values of ε_3.

a	ε_3	$\epsilon_{1,4}$	$\epsilon_{2,4}$	$\epsilon_{3,4}$	$\epsilon_{4,4}$	$\epsilon_{5,4}$	$\epsilon_{6,4}$	$\epsilon_{7,4}$	$\epsilon_{8,2}$	$\epsilon_{8,4}$
	0.24	1.66[+0]	8.38[−1]	2.02[−1]	6.59[−2]	4.58[−2]	5.02[−2]	3.63[−2]	4.91[−2]	2.34[−2]
0.9	−0.5	1.93[+0]	6.50[−1]	4.78[−2]	3.98[−1]	7.19[−2]	3.82[−2]	3.39[−2]	4.13[−2]	9.20[−3]
	−1.0	2.51[+0]	3.39[+0]	1.05[−1]	3.91[−1]	1.54[−1]	8.29[−2]	1.26[−1]	5.02[−2]	2.00[−2]

direction that one may have a situation where further extension of the expansion in only one of these directions leads to worse results. In this case, this behavior simply indicates that an increase of the expansion order in one direction should be accompanied also by the equivalent increase for the expansion in the other direction. Second, for all the values of ε_3 considered here, the relative error between the expanded and analytic shadows is $\lesssim 1\%$ already at the third order and this is already much smaller than the precision at which the measurements of the shadow will be carried out in practice.

In summary, although in principle the convergence of the parametrization cannot be analyzed in the general case, the examples considered with the Kerr-Sen (see Table I) and EDGB (see Table III) black holes show a clear convergence between the shadow from the expanded metric and that from the analytic metric. Furthermore, for the Johannsen-Psaltis metric, we observe convergence in both directions even for very large values of the deformation parameter ε_3 (see Table V). In particular, large positive values of this parameter, combined with rapid rotation, correspond to a shape of the event horizon that is highly prolate and close to its extreme form (further increases of this deformation lead to discontinuity of the horizon). At the same time, it is possible to study smaller negative values of the deformation parameter (which correspond to more oblate horizon shapes) that, in the case of rapid rotation, yield rather exotic event-horizon shapes, akin to a dumbbell. Yet, convergence is also observed for such exotic configurations, thus representing a convincing evidence that our parametrization suitably represents a wide class of axisymmetric black hole spacetimes.

V. CONCLUSIONS

We have introduced and subsequently employed a new method for performing general-relativistic ray-tracing calculations in order to calculate the black hole shadow images from a new parametrization of any axisymmetric black hole metric. This new parametrization can, with a small number of terms, represent any general stationary and axisymmetric black hole in any metric theory of gravity. We investigated and verified the effectiveness of this parametrization for successive orders in the expansion, demonstrating both its convergence and accuracy for three different spacetimes.

(1) The Kerr-Sen metric, fixed at second order in the polar expansion and varied from first through fourth order in the radial expansion (the Kerr black hole is exactly reproduced at second order in the polar direction).

(2) A regular form of the EDGB metric, itself obtained from an expansion in terms of the parameters χ and ζ. This regular solution is approximate but converges, to any desired accuracy, to the original approximate EDGB solution that diverges at $r=2M$. The expansion was purely polar and varied from first through fourth order (in $\cos^2\theta$) in the polar direction.

(3) The Johannsen-Psaltis metric, represented as a double expansion in both the polar and radial directions. The expansion was fixed at second order in the polar direction and varied from first to eighth order in the radial direction.

For all the aforementioned metrics, we chose values of the spin parameter and metric deformation parameters to be as extremal as possible while still ensuring the existence of an event horizon (i.e., avoiding the appearance of a naked singularity). We performed three tests for each expansion order of each metric, calculating the following: (i) the black hole shadow polar curve obtained at each order, (ii) the error relative to the exact metric along the shadow curve, and (iii) the error of the half-area of the black hole shadow with respect to that obtained from the exact metric.

Test (i) provided a qualitative comparison of the performance of the expansion as the order was increased, while test (ii) provided a quantification of the performance of the parametrization everywhere along the shadow boundary. This test, in particular, provided an understanding of how well the parametrization represents the spacetime, for example, in the equatorial plane and at the poles. Finally, test (iii) verified the excellent convergence behavior and accuracy of the parametrization as the expansion order was increased. We demonstrated that by increasing the order of polar and radial expansions the spacetime under consideration can be represented to essentially any desired accuracy [30].

Accurate calculations of black hole shadows in parametrized metrics represent a stringent test of parametrized representations of metric theories of gravity. Photons which delineate the shadow boundary pass very close to the event horizon and are subject to the steepest gradients of the gravitational potentials. Hence, accurately reproducing the behavior of the spacetime in these regions lends credence to the prospect of employing this parametrization framework to investigate not only black hole solutions in other metric theories of gravity, but to also perform the detailed radiative transport calculations required to investigate physical processes in other theories of gravity. Such calculations will prove useful for the interpretation of upcoming sub-mm VLBI observations from Sgr A* and for testing the Kerr black hole hypothesis.

[1] A. Eckart and R. Genzel, Nature (London) **383,** 415 (1996).

[2] S. Gillessen, F. Eisenhauer, S. Trippe, T. Alexander, R. Genzel, F. Martins, and T. Ott, Astrophys. J. **692,** 1075 (2009).

[3] A. Grenzebach, V. Perlick, and C. Lämmerzahl, Phys. Rev. D **89,** 124004 (2014).

[4] Arne Grenzebach, *The Shadow of Black Holes—An Analytic Description*, SpringerBriefs in Physics (Springer, Heidelberg, 2016).

[5] C. T. Cunningham and J. M. Bardeen, Astrophys. J. **183,** 237 (1973).

[6] C. Goddi, H. Falcke, M. Kramer, L. Rezzolla *et al.*, arXiv:1606.08879.

[7] L. Huang, M. Cai, Z.-Q. Shen, and F. Yuan, Mon. Not. R. Astron. Soc. **379,** 833 (2007).

[8] S. S. Doeleman *et al.*, Nature (London) **455,** 78 (2008).

[9] H. Falcke, F. Melia, and E. Agol, Astrophys. J. **528,** L13 (2000).

[10] L. C. Stein, Phys. Rev. D **90,** 044061 (2014).

[11] D. Ayzenberg and N. Yunes, Phys. Rev. D **90,** 044066 (2014).

[12] S. Vigeland, N. Yunes, and L. C. Stein, Phys. Rev. D **83,** 104027 (2011).

[13] L. Rezzolla and A. Zhidenko, Phys. Rev. D **90,** 084009 (2014).

[14] R. Konoplya, L. Rezzolla, and A. Zhidenko, Phys. Rev. D **93,** 064015 (2016).

[15] A. A. Abdujabbarov, L. Rezzolla, and B. J. Ahmedov, Mon. Not. R. Astron. Soc. **454,** 2423 (2015).

[16] Z. Younsi and K. Wu, Mon. Not. R. Astron. Soc. **454,** 3283 (2015).

[17] Z. Younsi, K. Wu, and S. V. Fuerst, Astron. Astrophys. **545,** A13 (2012).

[18] S. V. Fuerst and K. Wu, Astron. Astrophys. **424,** 733 (2004).

[19] H.-Y. Pu, K. Yun, Z. Younsi, and S.-J. Yoon, Astrophys. J. **820,** 105 (2016).

[20] J. Dexter, arXiv:1602.03184.

[21] X. Yang and J. Wang, Astrophys. J. Suppl. Ser. **207,** 6 (2013).

[22] C.-K. Chan, D. Psaltis, and F. Özel, Astrophys. J. **777,** 13 (2013).

[23] Z. Meliani, Y. Mizuno, H. Olivares, O. Porth, L. Rezzolla, and Z. Younsi, arXiv:1606.08192.

[24] B. Carter, Phys. Rev. **174,** 1559 (1968).

[25] W. H. Press, S. A. Teukolsky, W. T. Vetterling, and B. P. Flannery, *Numerical Recipes in FORTRAN. The Art of Scientific Computing*, 2nd ed. (Cambridge University Press, Cambridge, 1992).

[26] A. Sen, Phys. Rev. Lett. **69,** 1006 (1992).

[27] K. Hioki and U. Miyamoto, Phys. Rev. D **78,** 044007 (2008).

[28] T. Johannsen and D. Psaltis, Phys. Rev. D **83,** 124015 (2011).

[29] T. Okai, Prog. Theor. Phys. **92,** 47 (1994); A. Garcia, D. Galtsov, and O. Kechkin, Phys. Rev. Lett. **74,** 1276 (1995).

[30] See Supplemental Material at http://link.aps.org/supplemental/10.1103/PhysRevD.94.084025 for *Mathematica* notebooks containing the relevant coefficients for the metrics considered in this study.